TASK QUARTERLY 16 No 1, 33–51

LARGE-EDDY SIMULATIONS OF PARTICLE-LADEN TURBULENT JETS

MIROSŁAW ŁUNIEWSKI, PIOTR KOTULA
AND JACEK POZORSKI

Institute of Fluid-Flow Machinery, Polish Academy of Sciences,
Fiszera 14, 80-952 Gdansk, Poland
mirmir@imp.gda.pl, piotr.kotula@gmail.com, jp@imp.gda.pl

(Received 8 April 2012)

Abstract: The work presents an application of Large-Eddy Simulation (LES) for turbulent two-phase flows with dispersed particles. For the simulations of the continuous phase (fluid), an academic, finite volume LES solver was applied and customised. For comparison purposes, also a spectral solver was considered. The LES of fluid was used together with a Lagrangian module for the dispersed phase in the point-particle approximation, including the two-way momentum coupling between the phases. The particle solver has been further developed for parallel computations. The simulations of turbulent, particle-laden round jets were performed. The results for fluid and particle statistics were compared with available reference data.

Keywords: turbulence, large-eddy simulation, round jet, particle-laden flow

1. Introduction

With the advent of Computational Fluid Dynamics (CFD) in the 1960s and a continual increase in available computing power, it has become feasible to apply numerical methods also for the exploration of turbulent flows with the dispersed particles (solid inclusions, liquid droplets, or bubbles). Since particle-laden turbulent flows are often governed by unsteady, vortical structures, the Large-Eddy Simulation (LES) approach seems to be particularly well suited for the purpose, better than the statistical turbulence models [1]. On the other hand, because of its smaller computational cost, LES is a good alternative to the full solution of the flow, *i.e.*, the Direct Numerical Simulations (DNS). Yet, the LES method is still in development, and the more so for physically-complex situations, such as multiphase turbulence.

The present work is concerned with turbulent, two-phase jets. A significant progress in flow simulations has made it possible nowadays to use this tool for design and analysis purposes in the energy industry, chemical and process engineering, *etc.* Jet flows with the dispersed phase commonly occur in many

devices and systems, including sprays in combustion chambers of gas turbines and pulverised coal burners, spray cooling, spray dryers, *etc.* Typical geometrical configurations often involve coaxial jets (a central jet surrounded by one or more annular jets, particle-laden), and the LES studies are well justified both in "cold" (particle dispersion) [2] as well as "hot" (reactive flow) cases [3]. Despite some similarity features in the far field, the solutions of jet flows are, in general, sensitive to the geometrical configuration, inlet parameters, and the choice of other boundary conditions (outlet, side boundaries) [4]. For the sake of simplicity, and also because of computational cost, in the present study we deal with cold, single axisymmetric (rather than coaxial) jet flows.

The numerical studies of turbulent polydispersed flows have predominantly been based on RANS for fluid, in particular for industrial applications, because of the computational efficiency of the approach. Some recent developments and limitations of the statistical models are discussed in [5]. As far as statistical (RANS) simulations of jets are concerned, the Eulerian-Lagrangian approach with a stochastic particle dispersion model is often used. For example, Fan *et al.* [6] described the continuous phase (gas) with the $k-\epsilon$ turbulence model, and the particles were tracked using the mean fluid velocity and turbulent fluctuation statistics. In particular, the mean dispersion and velocity were obtained by averaging over a statistically significant number of particle trajectories.

Regarding the Eulerian-Lagrangian LES computations, Sbrizzai *et al.* [7] considered the dispersion of particles of different diameters and identified the flow structures which formed a three-dimensional, turbulent confined round jet. They completed the experimental evidence by other researchers [8] who observed particle clustering between vortex ring structures. In another LES study of particle-laden, axisymmetric turbulent jet, Almeida and Jaberi [9] investigated the effects of particle size, mass-loading ratio, and other flow/particle parameters on the statistics of both phases.

In the present work, we describe the computational approach, accounting also for the two-way momentum coupling between the phases, and report numerical results for turbulent jet flow with the dispersed particles. A hybrid Eulerian/Lagrangian approach was applied, with a CFD code for fluid LES coupled to the particle tracking module. A major part of the study involved parallel computations with the use of the MPI library, because of considerable CPU times required, in particular for multiple runs with some of the parameters varied.

2. Governing equations

2.1. Large Eddy Simulation of fluid flow

Regarding the carrier fluid, we consider an incompressible viscous flow in the absence of gravity. It is governed by the Navier-Stokes equations that in LES

are spatially-smoothed with a filter G of length scale $\bar{\Delta}$ and become the filtered equations for the resolved scales, or large eddies [1]:

$$\frac{\partial \bar{U}_i}{\partial t} + \bar{U}_j \frac{\partial \bar{U}_i}{\partial x_j} = -\frac{1}{\rho}\frac{\partial \bar{p}}{\partial x_i} + \nu \nabla^2 \bar{U}_i - \frac{\partial \tau_{ij}}{\partial x_j} + \frac{F_i}{\rho} \tag{1}$$

According to the idea of LES, flow variables are decomposed into resolved (large-scale) and residual (subgrid-scale) part: $\boldsymbol{U} = \bar{\boldsymbol{U}} + \boldsymbol{u}'$, $p = \bar{p} + p'$, *etc.*, where a symbol $(\bar{\cdot})$ stands for spatial filtering (smoothing), being a convolution: $\bar{\boldsymbol{U}} = G * \boldsymbol{U}$. In the filtered field, the flow scales smaller than a certain cut-off length (related to $\bar{\Delta}$) are eliminated. In Equation (1), τ_{ij} is the residual (subgrid-scale) stress tensor, $\tau_{ij} = \overline{U_i U_j} - \bar{U}_i \bar{U}_j$. The divergence of τ_{ij} represents the effect of small-scale velocity on the resolved flow. In the LES method, only larger scales of the motion are resolved, and smaller structures are represented by the so-called subgrid-scale model (SGS) that simulates their impact on the large-scale field. Typically, large flow structures transfer more energy than the small ones and are more susceptible to the influence of boundary conditions. The accuracy of LES predictions depends on the sound modelling of subgrid-scale interactions between phases and the correct representation of the initial/boundary conditions for all phases. Last, $\boldsymbol{F}$ on the right-hand side of Equation (1) refers to the force exerted by particles on the fluid (when applicable, *cf.* Section 2.3).

As seen from Equation (1), the large-eddy fluid dynamics is closed once a suitable model for the residual stress tensor is provided. For the present computation, the dynamic SGS model of Germano and Lilly (*cf.* [1]) has been applied. The deviatoric part of the residual stress tensor, $\tau_{ij}^d = \tau_{ij} - \tau_{kk}\delta_{ij}/3$, is modelled as:

$$\tau_{ij}^d = -2\nu_r \bar{S}_{ij} \tag{2}$$

where $\bar{S}_{ij}$ is the resolved strain rate (the symmetric part of the velocity gradient tensor). The residual, or sub-grid scale, viscosity ν_r is determined as $\nu_r = C_G \bar{\Delta}^2 |\bar{S}|$ where $|\bar{S}| = (2\bar{S}_{ij}\bar{S}_{ij})^{1/2}$ is the scale of the resolved strain rate. The dynamic procedure is applied for the Germano model coefficient C_G, computed from double filtering and subsequently averaged over the flow homogeneity directions.

2.2. Dispersed phase in the point-particle approximation

Point particle approximation is currently the most common and practically useful approach for particle-laden flows. Like in the Lagrange description, particle is treated as a mathematical point of mass, energy and momentum with independent velocity and location. Particle dynamics calculations are based on the Basset-Boussinesq-Oseen equations that assume large particle-fluid density ratio (over 10^3), no particle collisions and quite small particle diameter in relation to characteristic eddy length [10].

Generally, there are three regimes of coupling the dispersed phase with the continuous phase. First one, the simplest in implementation, is one-way momentum coupling (1-W), where the particle gets momentum from fluid with

no impact on fluid momentum. Second one, two-way momentum coupling (2-W), that takes into account the changes of fluid momentum because of particles. The last one, called four-way momentum coupling (4-W), includes also particle-particle interactions, in particular collisions. The choice of the appropriate regime depends on particle mass load and volume fraction, and on the kind of phenomena under consideration. The limits of applicability for each of the regimes (one-way, two-way, or four-way coupling) are illustrated in Figure 1 for the case typical of water drops in air, $\rho_p/\rho \sim 10^3$; the particle mass load in the flow is defined as $\alpha_M = \sum m_p/m$ and the volume fraction of the particulate phase is $\alpha_V = \sum V_p/V$.

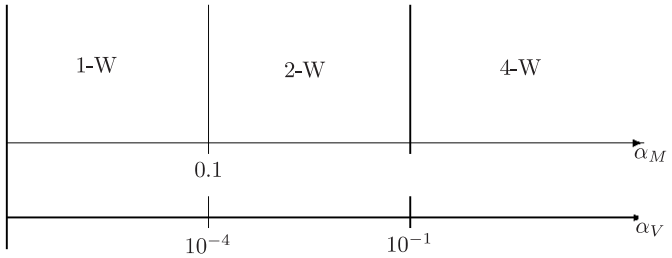

Figure 1. Applicability range of the one-way (1-W), two-way (2-W), and four-way (4-W) fluid-particle coupling regimes depending on the mass and volume fractions

In the following, the dispersed phase is treated as dilute, with the exception of Sections 2.3 and 4.3. For the dilute regime, the total particle mass load is relatively low so as not to affect the carrier fluid, and the one-way momentum coupling (fluid to particles only) is adequate. Also, because of the low particle volume fraction assumed, no particle-particle interactions are accounted for. The particle tracking approach is followed with a simplified particle equation of motion where only the drag term is retained [11]. This is generally accepted for the case of heavy particles, $\rho_p \gg \rho$. The drag force is based on the particle velocity $\boldsymbol{V}_p^n$, $n = 1,\ldots,N_p$, and the fluid velocity along particle trajectory, $\boldsymbol{U}_f^n(t) = \bar{\boldsymbol{U}}(\boldsymbol{x}_p^n, t)$. In the computation, $\boldsymbol{U}_f^n$ is interpolated from the large-eddy fluid velocity $\bar{\boldsymbol{U}}$ known at mesh points; trilinear interpolation is applied here. So, for the present case the equations of particle evolution are [11]:

$$\frac{d\boldsymbol{x}_p^n}{dt} = \boldsymbol{V}_p^n, \qquad \frac{d\,\boldsymbol{V}_p^n}{dt} = c_d^n \frac{\boldsymbol{U}_f^n - \boldsymbol{V}_p^n}{\tau_p}$$

The particle momentum relaxation time is defined as $\tau_p = (\rho_p/\rho)(d_p^2/18\nu)$; $c_d^n = 1 + 0.15(\mathrm{Re}_p^n)^{0.687}$ is the empirical drag correction factor; in this expression, $\mathrm{Re}_p^n = d_p|\,\boldsymbol{U}_f^n - \boldsymbol{V}_p^n|/\nu$ is the particle Reynolds number (based on the particle diameter d_p, the relative particle velocity, and the kinematic viscosity of the carrier fluid, ν). For the jet flow considered, the fluid convective time scale is $T_f = D_J/U_J$, and we introduce the Stokes number St (the particle inertia parameter) as the particle momentum relaxation time normalised with T_f, $\mathrm{St} = \tau_p/T_f$. In the two-way coupled regime, for a given particle number density, the higher St, the more the fluid motion is affected by the dispersed phase. Moreover, all flow results

in the following will be shown at time instants non-dimensionalised in this way: $t^+ = t/T_f$. In the present computation, particles are removed from the system upon the wall collision.

Although the LES of particle-laden flows is well-suited to simulate the gross features of the flow, specially for cases where the large flow scales control the particle motion, there is an ongoing debate as to the importance of the SGS fluid flow field on the dynamics of the particulate phase, *cf.* [12–14]. With the account of SGS fluid motions, the velocity "seen" by the particles would be taken as $\boldsymbol{U}_f^n + \boldsymbol{u}_f^n$, with the residual velocity "seen", $\boldsymbol{u}_f^n$, suitably modelled to account for the impact of the subfilter flow on the dispersed phase motion. In the present work, the SGS particle dispersion modelling is not considered.

2.3. Two-way momentum coupling

Implementation of the two-way momentum coupling starts with considering a momentum source term in the Navier-Stokes equation, Equation (1). The force per unit volume exerted by the particles on the fluid, $\boldsymbol{F}$, can be represented as the superposition of point forces at $\boldsymbol{x}_p^n = \boldsymbol{x}_p^n(t)$ (the Dirac deltas), with summation over all N_p particles [11]:

$$\boldsymbol{F}(\boldsymbol{x},t) = \sum_{n=1}^{N_p} \boldsymbol{f}_d^n(\boldsymbol{x}_p^n)\delta(\boldsymbol{x}-\boldsymbol{x}_p^n) \tag{3}$$

The individual particle contributions $\boldsymbol{f}_d^n$ will be the same (with the opposite sign) as the right-hand side terms in the particle equations of motion. The force that comes from a single particle drag contribution can be expressed as:

$$\boldsymbol{f}_d^n = m_p(\boldsymbol{V}_p^n - \boldsymbol{U}_p^n)\frac{c_d^n}{\tau_p} \tag{4}$$

where m_p is the particle mass. Now, coming to fluid, we apply the force definition in the N-S source term with appropriate smoothing of the delta contributions. For the sake of simplicity, we present the actual formula in 2D. In the case considered in the paper, the mesh surfaces in the streamwise (mean flow) direction are perpendicular to the jet axis, so interpolation of the particle source term in the third direction is straightforward. The force term becomes thus:

$$\boldsymbol{F}(\boldsymbol{x}_{ij}) = \sum_{n=1}^{N_p} \alpha_{ij}^n \left[(\boldsymbol{V}_p^n - \boldsymbol{U}^n(\boldsymbol{x}_p))\frac{c_d^n m_p}{\tau_p} \right] \tag{5}$$

where α_{ij}^n are the weight factors of particle source term with respect to the point $\boldsymbol{x}_{ij}$ (cell centre) where it enters the discretised fluid momentum equation.

In the simplest setting (zeroth order interpolation), the particle source term affects only the fluid in the very cell where the particle is located at a given time step. However, a more accurate technique (first order interpolation) is to redistribute the source terms over the neighboring centres of fluid cells. For the case of regular (cubicoidal) cells, this is just a tri-linear interpolation. However, for general, hexahedral cells, another method is proposed here, as illustrated in

Figure 2. There, the point P represents the particle location, $\boldsymbol{x}_P$, and the points A–D stand for the centres of fluid cells next to P. In particular, let $\boldsymbol{x}_{ij}$ be the coordinates of point A, *i.e.*, the centre of (i,j) cell from a given block of the mesh. Then, the weight factor of particle n with respect to A will be computed as the ratio of the area of the hatched quadrilateral in Figure 2 to the area of $ABCD$:

$$\alpha_{ij}^n = \frac{1}{2}\frac{(S_{PBC}+S_{PCD})}{S_{ABCB}}$$

Analogous formulae are used for the remaining weight factors in Equation (5); they are relatively straightforward to compute and not very costly in terms of CPU (the eight weight factors are needed for each particle at each time step).

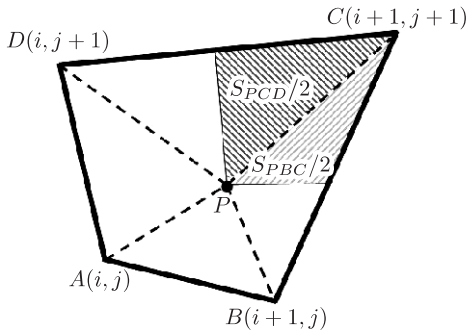

Figure 2. Schematic picture (2D) of particle source term distributed back to fluid; first order interpolation: particle P affects the 4 nearest cell centres

3. Numerical solution

3.1. Implementation issues

To compute the fluid flow, we mostly used a finite volume, academic solver of second-order accuracy (FASTEST3D code from TU Darmstadt, Germany). Some results were also compared to those obtained with another LES solver (spectral code SAILOR from the Częstochowa University of Technology). Since jets are open-type flows (with inflow and outflow), a pretty difficult part of the work was a reasonable choice of the computational domain together with suitable boundary conditions.

Next, the in-house Lagrangian particle solver PTSOLV, created for the channel flow case, was further developed and modified for dispersed jet flows. Several numerical issues were encountered and solved during these developments, including fast interpolation of the fluid velocity at particle locations on a non-Cartesian finite volume mesh, as well as efficient implementation of particles' exchange between blocks and processors in a multi-block, multi-processor computational setting. For example, interpolation in the outer blocks (uniform polar meshes) was straightforward (except in the cells next to the blocks' limits). Yet, for the central block whose mesh is not uniform (neither in Cartesian nor in the cylindrical co-

ordinates), another interpolation technique was conceived, with a pretabulation of fluid variables on a finer regular mesh at each time step.

Joined together, FASTEST3D and PTSOLV become a segregated solver for two-phase flows with one-way momentum coupling. To extend PTSOLV to the two-way coupling regime, the `pt2fluid` procedure was written to calculate the force source term for a particular fluid cell, depending on velocities and positions of particles, Equation (5). Values of source terms for fluid, kept in a global array, are applied at each iteration step of fluid solver through FASTEST3D procedure `caluvw`, dedicated to compute fluid velocity field. An analogy of buoyancy forces implementation has been used there.

Moreover, some parallelisation efficiency tests were performed. For the available parallel server and the problem at hand, it was found that the optimal number of processors was relatively low and, consequently, most of the runs were performed in the setup of 8 or 12 processors.

3.2. Geometry and grids

As to the choice of a suitable computational domain for round jet flows, the geometry (mesh) is either created in the Cartesian coordinates (x, y, z) or in the cylindrical system (r, θ, z); in both cases, z corresponds to the main flow direction. The Cartesian meshes have been used, *e.g.*, in [15–17]. As for the latter choice, the flow domain can be a cylinder [7, 18] or a truncated cone [19]. In the cylindrical geometry, the inlet section is sometimes added upstream of the jet orifice.

In view of our earlier experience with FASTEST3D code for fluid LES [20], the numerical mesh for single round jet was generated based on the cylindrical coordinate system. The computational domain in the radial direction r extended up to $R_{\max} = 3.5D_J$ where $D_J = 2R_J$ was the jet diameter at the inlet. The size of the domain in the streamwise (axial) direction z was $0 \le z \le 21D_J$, including a buffer zone of $3D_J$ close to the outlet. In the annular region $R_J \le r \le R_{\max}$, the mesh distribution in the radial and circumferential directions was uniform. In the streamwise direction, the mesh was uniform up to $18D_J$ and became gradually coarser in the outlet buffer zone as shown in Figure 3(a), resulting in 130 planes of finite volumes (FV). The mesh is of the block-structural type with the "O-grid" structure in r–θ plane. It is composed of the central block ($0 \le r \le R_J$, $0 \le \theta \le 2\pi$) surrounded by four "H-grid" blocks, $R_J \le r \le R_{\max}$, $i = 1,\ldots,4$, uniform in the polar coordinate system: $(i-1)\frac{\pi}{2} \le \theta \le i\frac{\pi}{2}$. Part of the mesh in the annular region possessed 60 FV in θ-direction and 20 FV in r-direction. The cross-section of the resulting computational mesh in r–θ plane is presented in Figure 3(b) and (c). Altogether, the mesh consists of 10 blocks: $1+4$ in the proper solution domain, $0 \le z \le 18D_J$, and the same in the outlet buffer zone.

On the other hand, the spectral code SAILOR for fluid LES used a single-block, Cartesian mesh [15]. For those simulations, the computational domain was: $-3.5D_J \le x \le 3.5D_J$, $-3.5D_J \le y \le 3.5D_J$, and $0 \le z \le 21D_J$. The mesh was

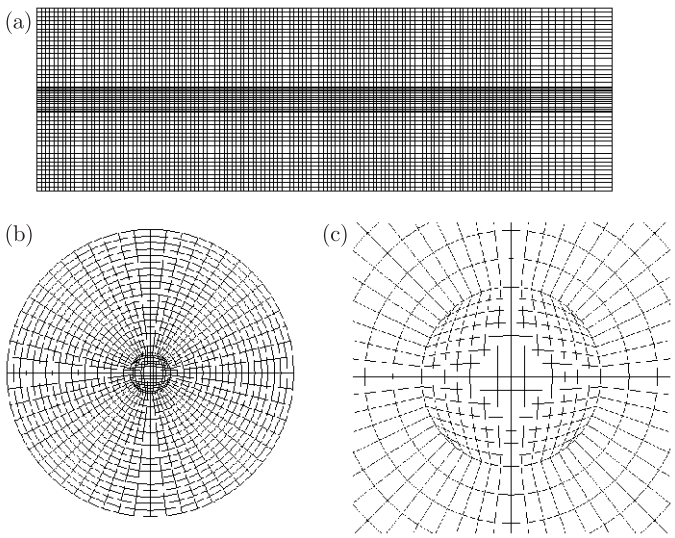

Figure 3. Block-structured mesh generated for the axisymmetric jet: (a) streamwise cross-section, (b) cross-stream section, (c) central part of the jet (zoom-in of (b))

uniform in all directions and consisted of $60\times60\times140$ nodes. Resulting size of a single FV was $\Delta x=\Delta y=\Delta\approx0.12D_J$ and $\Delta z\approx0.15D_J$.

3.3. Boundary conditions

The flow Reynolds number, $\mathrm{Re}_J=U_JD_J/\nu$, was defined with the inlet jet diameter D_J and the characteristic velocity of the jet at the inlet, U_J. For the flow of air (otherwise incompressible) with $U_J=4.1$ m/s and $R_J=0.05$ m, this resulted in $\mathrm{Re}_J=27\,500$.

The inlet velocity distribution of the jet was set with the hyperbolic tangent profile:

$$U_z(r,z=0)=\frac{U_J}{2}\left(1+\tanh\left[7.5\left(1-\frac{r}{R_J}\right)\right]\right) \tag{6}$$

In the inlet plane beyond the jet inlet, $R_J<R<R_{\max}$, and at the outer radial limit of the computational domain, $r=R_{\max}$, the wall boundary conditions were assumed. This resulted in the jet being confined with consequent repercussions for the flow picture, as shown later in the paper.

In the flow outlet plane, $z=21D_J$, the convective outlet boundary condition was applied:

$$\frac{\partial U_z}{\partial t}+U_c\frac{\partial U_z}{\partial z}=0 \tag{7}$$

where U_c is the bulk velocity at the outlet. In the course of simulations we found that the convective boundary condition was sensitive to size of the computational domain in the axial direction. For one of the preliminary meshes constructed, with the total length of the domain of $z_{\max}=14D_J$ (out of that, $2D_J$ was the length of the buffer zone), in the outlet flow region the convective b.c. generated considerable gradients of fluid velocity components perpendicular to

the streamwise direction. As a result, close to the outer radial boundary, $r = R_{\max}$, a recirculating flow region appeared with $U_z < 0$. An increase of the domain up to $z_{\max} = 21D_J$ allowed the convective outlet b.c. to work correctly (with no backflow).

For the spectral LES solver SAILOR, the boundary conditions were slightly different. At the inlet, the mean velocity profile (6) was superposed with the fluctuating velocity of intensity at the level of 1% of U_J. On the side limits of the computational domain, for $x = \pm 3.5D_J$ and $y = \pm 3.5D_J$, periodic boundary conditions were applied. In the inlet plane beyond the jet inlet area, the coflow velocity of $0.05U_J$ was assumed. At the outlet, the convective b.c. (7) was applied.

4. Results for single axisymmetric jet

4.1. One-way coupling: results for fluid

Calculations were performed up to $t^+ = 3690$ with the time step of $\Delta t^+ = 0.0123$ (which translates to about 300000 iterations). The statistically-steady state was reached at $t^+ = 2460$ and since that time instant the averages (*cf.* below) were gathered. A typical picture of the instantaneous flow field is presented in Figure 4 as the color map of the streamwise velocity component resulting from both fluid LES codes used.

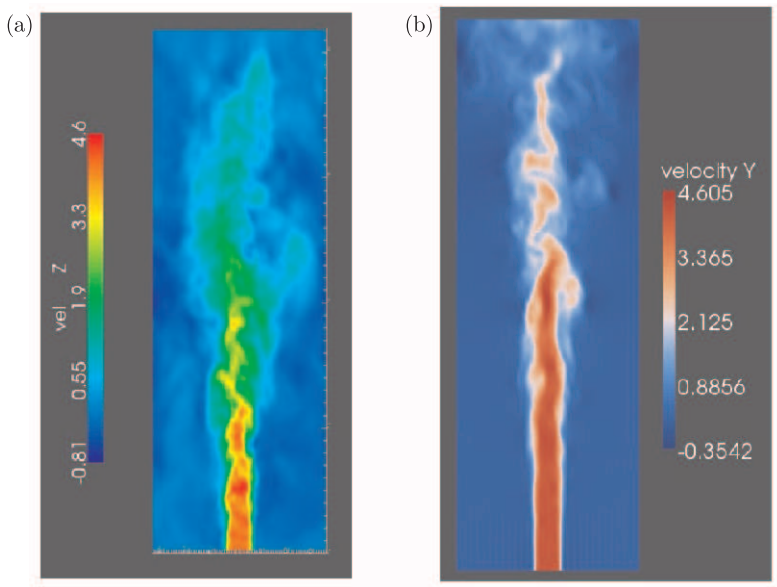

Figure 4. Instantaneous flow field of the single jet – a map of the streamwise velocity component. Velocity snapshots at the end of the simulation, in the axial cross-section: (a) the finite volume LES solver FASTEST3D; (b) the spectral LES solver SAILOR

Next, to collect statistics of velocity, the averaging procedure was adopted, as follows. For any hydrodynamic variable $Q_{\text{cart}}(x,y,z,t) = Q_{\text{cyl}}(r,\theta,z,t)$, ensemble averages in a statistically steady state become independent of the angular

coordinate (because of the axial symmetry of the statistical one-point moments of the flow variables), $\langle Q\rangle = \langle Q\rangle(r,z)$, and are approximated by the time averages:

$$\langle Q\rangle(r,z) \approx \frac{1}{2\pi\Delta t_{\rm avg}} \int_t^{t+\Delta t_{\rm avg}} dt \int_0^{2\pi} d\theta\, Q(r,\theta,z,t) \tag{8}$$

In practical terms, the averaging time was taken as $\Delta t^+_{\rm avg} = 615$ for the present case. The averages, defined and computed in the above way, have been determined as radial profiles for a a few axial coordinates z, *i.e.*, at selected downstream stations of the round jet.

Obviously, both for flow variables and for the particle data (shown in the next subsection), their values are known only at some, discrete set of radial coordinates r. Therefore, to produce mean radial profiles, the method of discretising ("binning") the r–interval had to be conceived. Actually, three different variants were proposed to discretise the interval $0 \le r \le R_{\rm max}$ where $R_{\rm max} = 3.5D_J$ was the size of "the computational cylinder". The first variant, called "avg1", consisted in selecting the limits of consecutive r–bins so that approximately the same number N of points (either the centres of FV, for fluid averages, or particles) was found in each bin. Alternatively, the second variant ("avg2") used equal bin sizes, and in the last one ("avg3") the limits of r–bins were determined to produce approximately equal areas of individual cross-sections (the central circle and consecutive annuli).

The computed histograms of the distribution of nodal points (x_i, y_i) being, again, either the centres of FV or particles, are shown in Figure 5 for all three variants of binning applied. As readily seen, the simplest way of defining bins of equal size ("avg2") results in a different number of samples in each sub-interval and, consequently, produces a radially-varying level of the statistical error, which is undesirable, whereas the remaining two variants produce a roughly equal number of samples in each sub-interval. This is obviously the consequence of the nodal locations being statistically uniformly distributed in the cross-section. The situation will become more difficult to manage for the non-uniform distribution of points (either the FV centres or particles); this will be reflected in the statistical error level of radial profiles, as illustrated in the next subsection. Moreover, the statistical noise level of the computed profiles will decrease with the decreasing number of bins. However, this will occur at the expense of spatial resolution and a compromise has to be worked out on a per-case basis.

Next, important information about the jet flow can be gathered by identifying the so-called potential core (PC) of the jet. This is the region close to the inlet where the axisymmetric mixing layer at R_J has not yet developed (down in r) to reach the jet centerline (CL). The length of the potential core, z_{PC}, as measured from the jet inlet plane $z = 0$, is defined by the mean velocity at the jet centerline, $U_{CL}(z)$, in a way analogous to the usual definition of the boundary (or mixing) layer thickness:

$$U_{CL}(z) \equiv \bar{U}_z(r=0,z) = 0.95U_J \tag{9}$$

This quantity can be readily determined from the mean axial velocity at the symmetry axis, as shown in Figure 6. The potential core length for the finite volume LES code is $z_{PC} \approx 3.5 D_J$ and for the spectral code $z_{PC} \approx 8.4 D_J$ which compares better with the experimental data of Crow and Champagne [21] that predict $z_{PC} \approx 6 D_J$. A possible explanation of this discrepancy may be twofold: a better accuracy of the spectral solver, but also a different specification of the flow boundary condition at the outer radial boundary (the wall b.c. as opposed to the periodic b.c. with co-flow). In the former case, secondary flows appear in the vicinity of the side boundary and may reduce the length of the core jet.

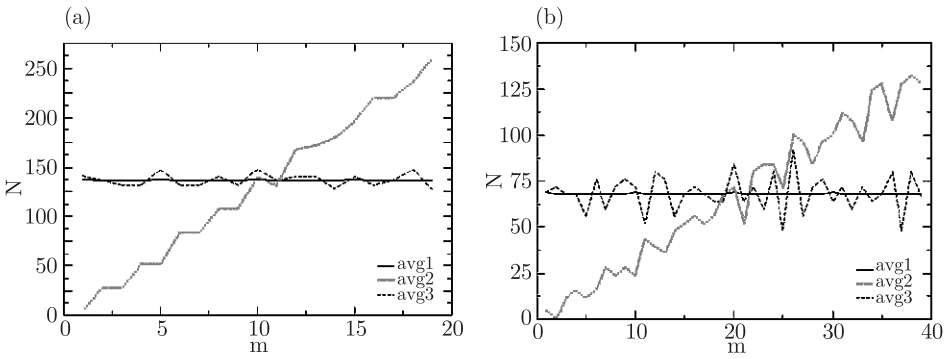

Figure 5. The histograms of the number of "realisations", *i.e.*, the number of nodal values occurring in the discretisation for averaging along the r-direction: (a) for 20 bins (subintervals in r), (b) for 40 bins. Discretisation variants of the radial coordinate: 'avg1' – equal number of realisations that fall into each bin; 'avg2' – equal-size bins; 'avg3' – equal-area cross-sections (annuli)

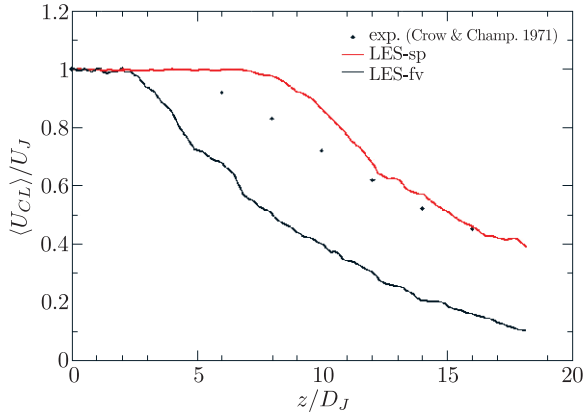

Figure 6. The mean axial velocity vs. the streamwise coordinate; fv – finite-volume LES solver (FASTEST3D), sp – spectral LES solver (SAILOR)

Figure 7 shows the radial profiles of the mean axial velocity component, $\bar{U}_z(r/R_J)$, normalised with the jet inlet bulk velocity. The profiles are given at four downstream stations, of z equal to D_J, $6D_J$, $12D_J$, and $18D_J$. As before, *cf.* also (8), the velocity component was averaged in time and over the angular

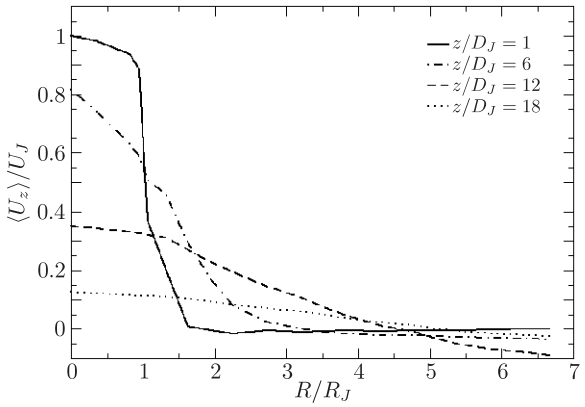

Figure 7. The radial profiles of the mean axial velocity at selected streamwise stations

coordinate. A gradual decrease of the jet centerline velocity, and the increase of the jet width are readily noticed.

An often invoked hypothesis about jets (and other free-shear flows) is that of self-similarity. To check whether the LES computation yields self-similar mean velocity profiles (except in the near field where the details of the jet inlet play a predominant role), we first determined the jet half-width R_{12}, defined from:

$$\bar{U}_z(r{=}R_{12},z) = \frac{1}{2}\bar{U}_z(r{=}0,z) = \frac{1}{2}U_{CL}(z) \tag{10}$$

As illustrated in Figure 8, the radial profiles of the mean axial velocity, normalised with the relevant velocity scale, $U_{CL}(z)$, indeed exhibit the self-similarity feature and compare favourably with the experimental data of Panchapakesan & Lumley [22]. Negative values of $\bar{U}_z$ at larger r are due to the secondary, recirculating flow close to the outer radial boundary (with the wall b.c. assumed there).

Next, we computed second-order velocity moments. For example, the intensity, or r.m.s., of the fluctuating axial velocity component is found from:

$$u'_{z,\mathrm{r.m.s.}} = \langle (U_z - \langle U_z \rangle)^2 \rangle^{1/2} \tag{11}$$

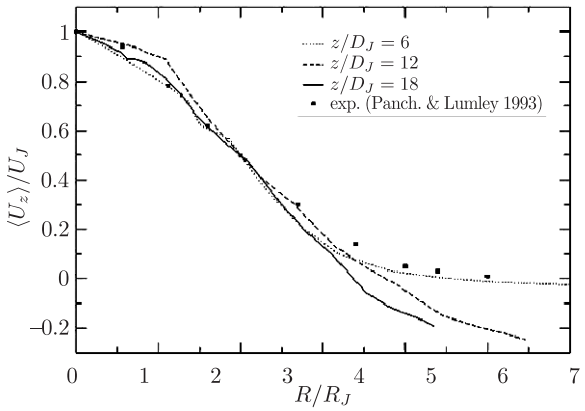

Figure 8. Self-similar character of the mean axial velocity profiles

where the averaging operator $\langle\cdot\rangle$ has already been defined in Equation (8).

Figure 9 shows the radial profiles of the fluctuating axial velocity r.m.s., normalised with the self-similarity variables. The profiles are computed for both LES codes at several stations downstream of the jet inlet. Here, the results show considerable scatter but, once again, the agreement of the spectral code predictions with the experiment [22] is better. The increase of the normalised turbulent kinetic energy with distance downstream is readily noticed. Unfortunately, the experimental reference data are too scarce to more accurately validate the computations of the second-order velocity statistics.

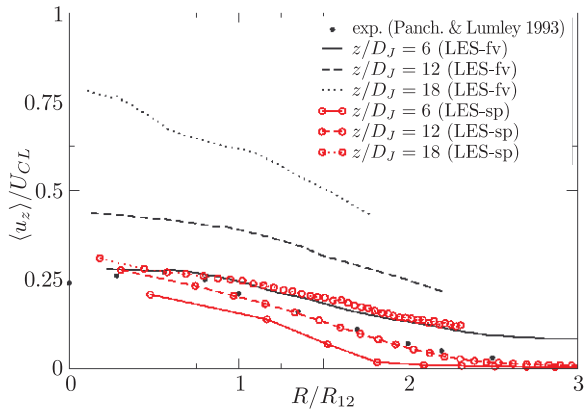

Figure 9. The radial profiles of the r.m.s. fluctuating axial fluid velocity at several downstream stations of the single jet. The results for two LES solvers: finite volume (fv) and spectral (sp)

4.2. One-way coupling: results for particles

Once a statistically-steady fluid flow field had been obtained, heavy particles were added to the flow, at a rate of 10 particles per time step, uniformly distributed over the jet inlet area. Particle initial velocity is set equal to the instantaneous fluid velocity at the jet inlet. The particle evolution equations, presented in Section 2, contained the drag term only (no lift force, no subfilter dispersion modelling for the time being). The particle to fluid density ratio was $\rho_p/\rho_f = 769$, corresponding to water drops in air. The particle diameters were chosen so that four classes of monodispersed particles were tracked in separate runs. The particle Stokes numbers St were taken equal to 1, 5, 25, and 125. This resulted in the particle inertia parameters ranging from small ones (behaving close to fluid particles), up to inert ones (hardly responding to the flow).

The evolution of the total particle number in the computational domain for all St and for the two LES solvers is shown in Figure 10. It is readily noticed that the total particle number depends on the particle inertia parameter (St), with smaller particles prone to accumulate in the domain. Also, the accumulation of particles depends considerably on the kind of boundary condition applied at

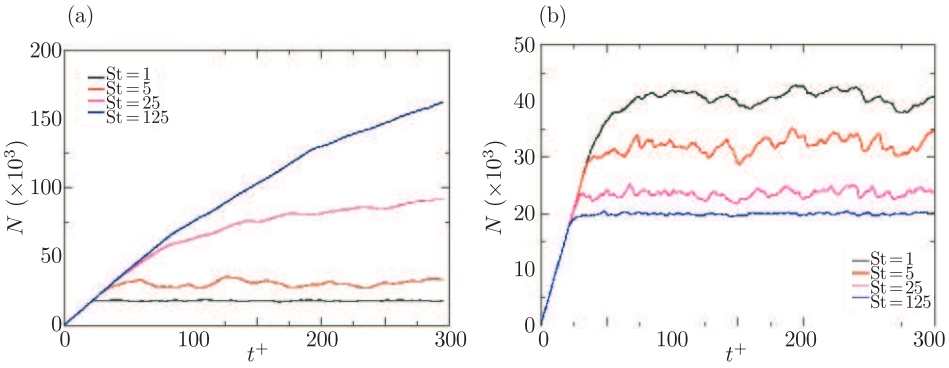

Figure 10. Temporal evolution of the total particle number in the computational domain. Effect of the boundary condition at the domain side: (a) wall b.c. for FASTEST3D solver, (b) periodic b.c. with co-flow for SAILOR solver

the side boundary of the domain: either wall b.c. at $r = R_{\max}$ for the cylindrical domain used in FASTEST3D, or periodic b.c. with co-flow at $|x| = |y| = 3.5D_J$ for the square domain in SAILOR. Consequently, the type of the side b.c. influences not only the fluid velocity statistics (with recirculating regions present for the side wall b.c.), but also heavily impacts on the particle flow picture for smaller-inertia particles. In the particle-laden flow computed with FASTEST3D fluid velocity and side wall b.c., the small inertia particles hardly attain a steady-state number in the flow domain, since they tend to increasingly accumulate in the recirculation region and slowly migrate upstream, next to the outer radial boundary.

This feature is better seen on the radial profiles of instantaneous particle concentration, Figure 11(a). For three cross-sections, perpendicular to the jet axis, the concentration exhibits a decreasing maximum at the centerline (naturally due to the inlet b.c.), but also local maxima close to the radial outer boundary, because

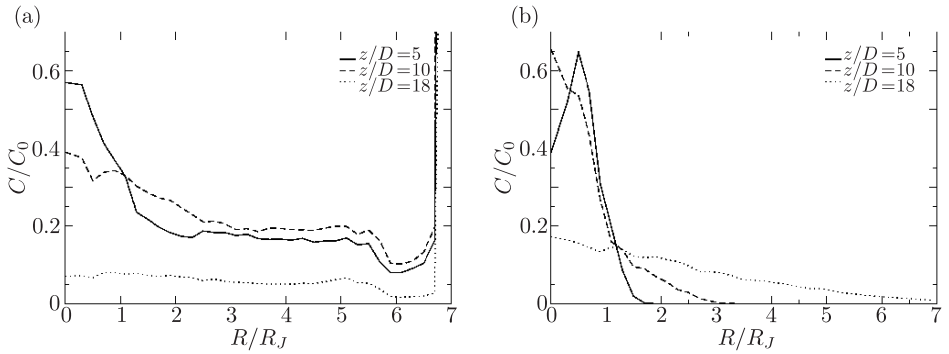

Figure 11. Radial profiles of particle concentration, effect of the flow boundary condition at the side boundary in LES: (a) wall boundary condition at the outer radial surface (finite-volume solver); (b) periodic boundary condition with co-flow at the side boundaries (spectral solver). C_0 stands for the mean particle number density (concentration) in a given cross-section

of the particle accumulation in the near-wall region. This can also be observed on the plots of instantaneous particle locations in the jet, Figure 12, where the axial cross-sections of the jet are shown next to the cross-stream section at the jet outlet. It is visible from the pairs of plots that the larger particles tend to stay focused close to the jet centerline whereas the smaller ones get more easily dispersed in the flow domain and, because of the side wall b.c., even migrate upstream. For the particle motion, the deposition condition is applied at the walls, but (because of the fluid velocity being small there), the particles tend to stay longer next to the walls.

The situation is different for the spectral LES simulations (SAILOR solver) with co-flow condition at the side boundaries. There, the concentration profiles are monotonic, with a single maximum at the jet centerline, *cf.* Figure 11(b).

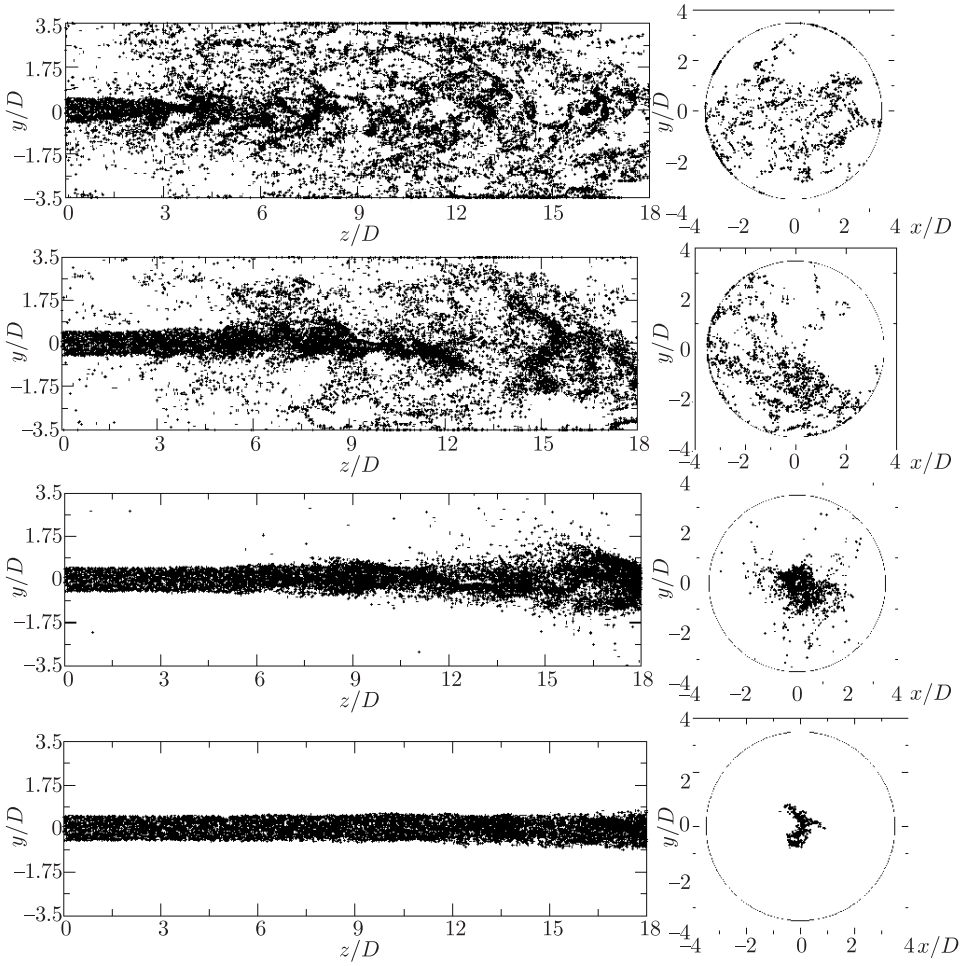

Figure 12. Particle snapshots in single axisymmetric jet. Left plots: axial cross-sections of the jet, right plots: cross-sections perpendicular to the jet axis, located at the jet outlet ($z/D_J = 18$). Plot pairs, from the top to the bottom: particles of St = 1, 5, 25, and 125

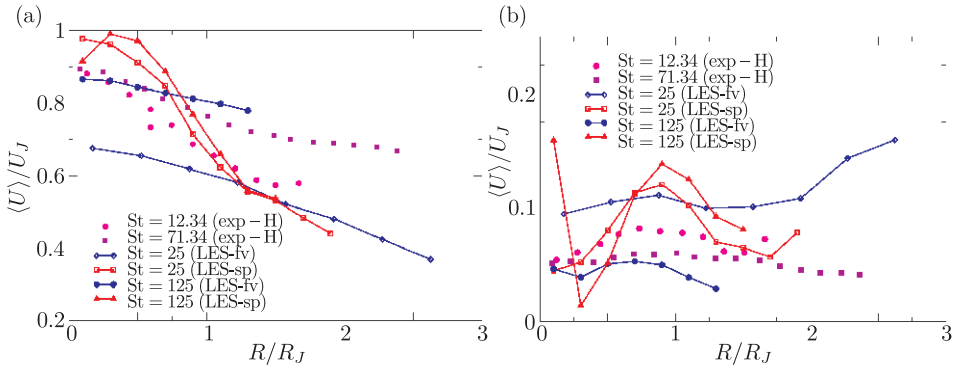

Figure 13. Particle velocity statistics in single axisymmetric jet: (a) normalised mean axial velocity; (b) normalised r.m.s. fluctuating axial velocity. Radial profiles at $z/D_J = 10$

Particle velocity statistics, and specially their radial profiles, have been computed in the same way as done (and explained) for fluid, *i.e.*, using the r-bins. Yet, here the problem arises because the particle concentration (contrary to the distribution of FV centres for fluid statistics) is far from uniform, specially for larger-inertia particles and at the locations closer to the jet inlet. Therefore, the particle statistics will exhibit considerable unphysical scatter at larger r-stations, unless specific measures are adopted.

The resulting particle velocity statistics: the mean axial velocity and the r.m.s. fluctuating axial velocity at $z/D_J = 10$ are plotted in Figure 13. The results are compared with available experimental data of Hishida *et al.* [23]. NB: the experiment was performed for particle St numbers differing from ours, but the fluid flow data were kept close to each other. The lack of comprehensive, relevant reference data set makes a full comparative analysis more difficult.

4.3. Results for two-way coupling

In this simulation variant, particle initial velocities were set to zero at the jet inlet. The influence of the particle source term is made visible by analyzing fluid velocity profiles taken at the jet axis. Figure 14 shows the difference between the velocity field of turbulent flow non-disturbed by dispersed phase (1-way coupling) and the velocity fields with momentum coupling for two orders of interpolation. For middle-size particles (St = 25), the particle mass load was $\alpha_M = 0.31$ (mean value in the flow domain), whereas for larger ones (St = 125), it was $\alpha_M = 2.72$. One can notice that momentum is taken from the fluid upstream, near the inlet zone, and is returned to fluid in the downstream region, where the non-affected fluid slows down. Also, some systematic difference between zeroth- and first-order interpolation results in two-way coupled case is seen, specially for larger particle mass load. These results are in line with a recently published, comprehensive analysis of a cold combustion chamber flow [24] where also the 4-way coupling effects (interparticle collisions) are studied.

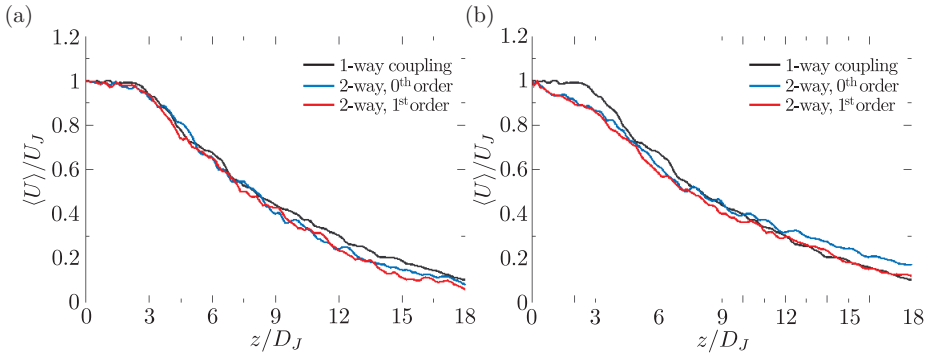

Figure 14. Impact of the dispersed phase on the mean fluid velocity along the jet centerline: (a) St = 25, (b) St = 125. Differences between interpolation schemes; heavy particles with zero inlet velocity

5. Concluding remarks

In the present work, detailed LES studies of the particle-laden, turbulent jets were performed. The LES of round jets were mostly carried out with the finite volume discretisation of flow equations on a 10-block mesh. Some computations were also done with the spectral method. In the resulting fluid velocity field, the equations governing the motion of the dispersed phase were integrated. A substantial difficulty was the coupling of both LES codes for fluid with our own Lagrangian module for particle tracking, worked out for channel flows and further developed here for jet flows. The difficulties were mainly due to certain aspects of parallel computations with the multiblock solver, and, in some measure, also with the efficient interpolation routines for the carrier phase (fluid) quantities at the particle locations.

An extensive collection of LES results was produced for single-phase and dispersed jets. Presented results, in particular the statistics for the carrier phase, indicate the existence of strong secondary flows near the wall. Those secondary flows are likely due to the choice of the limited computational domain for the considered turbulent jet. Results for the dispersed phase in a simple axisymmetric jet were compared against available reference data. Although the quantitative results are not perfect, acquired experience for particle-laden jets allowed us to work out some hints for this class of flows, regarding the choice of the mesh, boundary conditions, time of computations and statistical averaging of results. The recommendations may also prove useful for LES of coaxial jets and, ultimately, the two-phase combustion (liquid fuel spray, pulverised coal) in jet configurations occurring in combustion chambers of gas turbines and industrial boilers.

We have studied the particle-laden flow with one-way and two-way momentum coupling between the phases. For the latter variant, we have also shown the influence of first-order (quasi-linear) interpolation of the source term over fluid cells. The results convincingly show the impact of the two-way coupling for sufficiently high particle mass load.

The LES studies of single jets have revealed to be quite demanding (specially in terms of the CPU time). Also, the side boundary of the jet appears to play a considerable role. We have documented this feature by running two solvers for fluid LES: one with the side wall b.c., and the other one with the periodic co-flow boundary. Boersma *et al.* [4] report the successful use of another kind of b.c., called there "traction free" condition. It seems to be a worthwhile (although not evident) endeavour to implement this kind of b.c. in (one of) the fluid LES codes used here.

Acknowledgements

We thank Prof. Michael Schäfer (TU Darmstadt, Germany) for a licence agreement to use and further develop FASTEST3D code for fluid LES. We also wish to thank Dr. Artur Tyliszczak (Częstochowa University of Technology) for his spectral LES code SAILOR for fluid, applied in some jet simulations. We are grateful to Dr. Marta Wacławczyk who developed some numerical routines for coupling the spectral code SAILOR to the particle solver and studied single-phase LES with FASTEST3D code at the first stage of the work. Also, the assistance of Mr. Arkadiusz Grucelski (the particle exchange schemes in parallel programming) and Mrs. Maria Knorps (part of the post-processing routines for velocity averaging) is kindly acknowledged. Some simulation runs have been carried out at the regional Academic Computer Centre (TASK) at Gdansk, Poland.

References

[1] Pope S B 2000 *Turbulent Flows*, Cambridge University Press
[2] Apte S V, Mahesh K, Moin P and Oefelein J C 2003 *Int. J. Multiphase Flow* **29** 1311
[3] Moin P and Apte S V 2006 *AIAA J.* **44** 698
[4] Boersma B J, Brethouwer G and Nieuwstadt F T M 1998 *Phys. Fluids* **10** 899
[5] Peirano E, Chibbaro S, Pozorski J and Minier J P 2006 *Prog. Energy Combust. Sci.* **32** 315
[6] Fan J, Zhang X, Chen L and Cen K 1997 *Chem. Engng J.* **66** 207
[7] Sbrizzai F, Verzicco R, Pidria M F and Soldati A 2004 *Int. J. Multiphase Flow* **30** 1389
[8] Longmire E K and Eaton J K 1992 *J. Fluid Mech.* **236** 217
[9] Almeida T G and Jaberi F A 2008 *Int. J. Heat Mass Transfer* **51** 683
[10] Brennen C E 2005 *Fundamentals of Multiphase Flow*, Cambridge University Press
[11] Squires K D 2007 *Computational Methods for Multiphase Flow*, (Prosperetti A and Tryggvason G, Eds) Cambridge University Press
[12] Fede P and Simonin O 2006 *Phys. Fluids* **18** 45103
[13] Pozorski J and Apte S V 2009 *Int. J. Multiphase Flow* **35** 118
[14] Pozorski J and Łuniewski M 2008 *Quality and Reliability of Large-Eddy Simulations*, (Meyers J, Geurts B and Sagaut P, Eds) Springer, pp. 331–342
[15] Tyliszczak A, Bogusławski A and Drobniak S 2008 *Quality and Reliability of Large-Eddy Simulations*, (Meyers J, Geurts B and Sagaut P, Eds) Springer, pp. 259–270
[16] Bogey C and Bailly C 2006 *Int. J. Heat Fluid Flow* **27** 603
[17] Uzun A, Blaisdell G A and Lyrintzis A S 2004 *J. Sci. Comput.* **21** 283
[18] Wang P, Fröhlich J, Michelassi V and Rodi W 2008 *Int. J. Heat Fluid Flow* **29** 654
[19] Boersma B J 2005 *Theoret. Comput. Fluids Dynamics* **19** 161

[20] Pozorski J, Wacławczyk T and Łuniewski M 2007 *J. Theor. Appl. Mech.* **45** 643
[21] Crow S C and Champagne F H 1971 *J. Fluid Mech.* **48** 547
[22] Panchapakesan N R and Lumley J L 1993 *J. Fluid Mech.* **246** 197
[23] Hishida K, Takemoto K and Maeda M 1987 *Jap. J. Multiphase Flow* **1** 56
[24] Breuer M and Alletto M 2012 *Int. J. Heat Fluid Flow* **35** 2